

## Circular Geometry in Molecular Stream Separation to Facilitate Nonorthogonal Field-to-Flow Orientation

Sven Kochmann,<sup>1</sup> Nikita A. Ivanov,<sup>1</sup> J. C. Yves Le Blanc, Boris I. Gorin, and Sergey N. Krylov\*Cite This: *Anal. Chem.* 2022, 94, 9519–9524

Read Online

ACCESS |



Metrics &amp; More

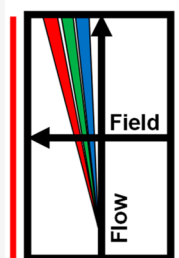
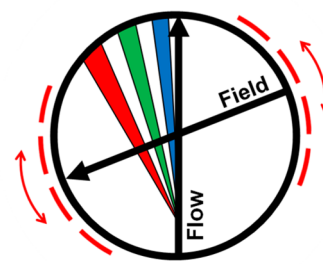


Article Recommendations



Supporting Information

**ABSTRACT:** Molecular stream separation (MSS) is a promising complement for continuous-flow synthesis. MSS is driven by forces exerted on molecules by a field applied at an angle to the stream-carrying flow. MSS has only been performed with a 90° field-to-flow angle because of a rectangular geometry of canonic MSS; the second-order rotational symmetry of a rectangle prevents any other angle. Here, we propose a noncanonic circular geometry for MSS, which better aligns with the polar nature of MSS and allows changing the field-to-flow. We conducted *in silico* and experimental studies of circular geometry for continuous-flow electrophoresis (CFE, an MSS method). We proved two advantages of circular CFE over its rectangular counterpart. First, circular CFE can support better flow and electric-field uniformity than rectangular CFE. Second, the nonorthogonal field-to-flow orientation, achievable in circular CFE, can result in a higher stream resolution than the orthogonal one. Considering that circular CFE devices are not more complex in fabrication than rectangular ones, we foresee that circular CFE will serve as a new standard and a testbed for the investigation and creation of new CFE modalities.

Rectangular  
OrthogonalCircular  
Nonorthogonal

Continuous-flow organic synthesis has several important advantages over its batch counterpart,<sup>1–3</sup> and continuous separation is its logical extension.<sup>4–6</sup> There are several continuous-separation methods; however, the only widely used one is liquid–liquid extraction, which can barely separate multiple species from each other.<sup>7,8</sup> In contrast, molecular stream separation (MSS) can continuously separate multiple species, although its early stage of development hinders the efficient combination with continuous-flow synthesis.<sup>9–11</sup> MSS is driven by a force exerted discriminatively on the separated species by a force field oriented at an angle to the hydrodynamic flow carrying the streams. The interplay of the separating force and the hydrodynamic flow causes the splitting of the stream of mixed species into their individual molecular streams (Figure 1a).

Fundamentally, MSS is defined by three variables: field-to-flow angle, field strength, and flow rate. The influence of the varying magnitudes of field strength and flow rate on MSS has been extensively studied, and these parameters are used to control separation.<sup>12</sup> On the opposite side, the field-to-flow angle has always been 90° due to the apparent obviousness that the 90° angle is optimal as well as conceptual challenges and technical difficulties associated with the nonorthogonal field-to-flow orientation within the canonic rectangular paradigm of MSS (as is discussed below).<sup>13</sup> The aim of this work was to understand if the field-to-flow orientation can be included as a degree of freedom, thus facilitating non-orthogonal MSS for exploration and potential use.

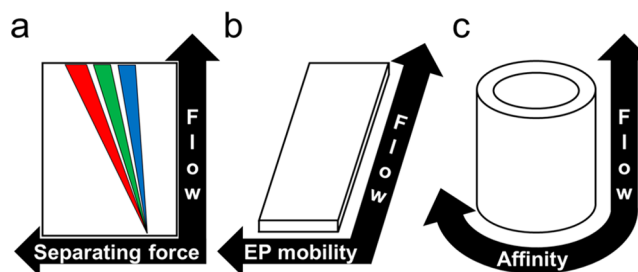


**Figure 1.** Schematic depiction of conventional orthogonal MSS: (a) general principle and its implementation in (b) continuous-flow electrophoresis (CFE) with differential electrophoretic (EP) mobility of molecules being the driving force of MSS and (c) continuous annular chromatography (CAC) with differential affinity to the solid phase driving MSS.

There are two major MSS methods: continuous-flow electrophoresis (CFE, Figure 1b) and continuous annular chromatography (CAC, Figure 1c).<sup>14,15</sup> Both CAC and CFE utilize a rectangular geometry; the rectangle is planar for CFE

Received: April 26, 2022

Accepted: June 24, 2022

Published: June 29, 2022



and folded into a cylinder for CAC. In CFE, two straight parallel electrodes constitute two sides of a thin rectangular separation zone in which the electric field is perpendicular to the hydrodynamic flow. In CAC, a thin cylindrical layer of the chromatographic stationary phase is rotating orthogonally to the hydrodynamic flow creating an infinitely long stationary phase and a continuous force field.

The rectangular geometry of canonic MSS does not allow the change of the field-to-flow angle because of the second-order rotational symmetry of a rectangle (Figure 2a). A

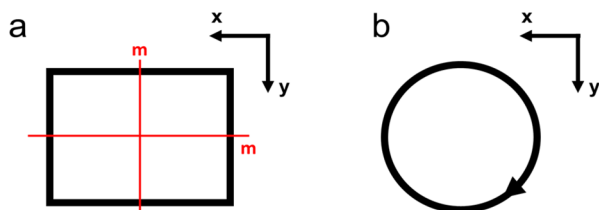


**Figure 2.** Illustration of (a) second-order rotational symmetry for conventional rectangular-geometry MSS and (b) high-order rotational symmetry for hypothetical circular-geometry MSS. A rectangle has two mirror axes, and a circle has an infinite number of mirror axes in the  $x$ - $y$  plane.

rectangle has only two equivalent rotational positions and allows only orthogonal field-to-flow orientation. To allow all field-to-flow angles, the geometry must be of the infinite-order symmetry, i.e., circular rotational symmetry (Figure 2b). This symmetry would be in alignment with the polar system of coordinates and angulagrams recently introduced for description of MSS.<sup>16</sup>

Note that the circular symmetry transforms into spherical symmetry for CAC due to CAC utilizing a folded rectangle (Figure S1). The relative simplicity of a planar circular MSS device over a spherical one predefined our choice of circular CFE over spherical CAC for this experimental work.

In an ideal CFE device, the electric field and the hydrodynamic flow should be uniform, i.e., field and flow lines must be straight, parallel, and uniformly spaced inside most of the separation zone. Intuitively, a classic rectangular device with straight and parallel electrodes and a rectangular separation zone between them is best to satisfy the uniformity condition. In contrast, a circular device, having arc-shaped electrodes circularly oriented around a circular separation zone, a priori appeared to be completely incompatible with the uniformity requirement. The major goal of our investigation was to understand if circular-geometry CFE was feasible; i.e., a working proof-of-concept device could be created with the same simple-to-use fabrication process that we developed before.<sup>17</sup>

Developing a circular CFE device with both a uniform field and a uniform flow requires a quantitative measure of uniformity. We used an index of uniformity  $\Gamma$  which provides the relative degree of uniformity inside the separation zone of our CFE device with a maximum value of  $\Gamma$  being unity (Note S1).

This study requires evaluating multiple hypotheses via testing multiple CFE device designs. We use a milling process to fabricate CFE devices.<sup>17</sup> Making one device takes a day and incurs a non-negligible cost in materials and supplies. Accordingly, this study could become impractically long and/or cost prohibitive if carried out experimentally only. To keep

the project within reasonable time and cost scales, we investigated multiple virtual devices within COMSOL Multiphysics software. Modeling in COMSOL allowed us not only to assess the feasibility of circular CFE but also to optimize the design of a CFE device before fabricating it. The details of our COMSOL model can be found in Note S2.

The hydrodynamic flow and the electric field do not interfere with each other in the first approximation. Hence, we consider their uniformity separately starting with the flow uniformity. As an initial point, we selected the design with a circular separation zone of uniform thickness and a single source and sink for the flow (Figure 3a). Expectedly, the flow

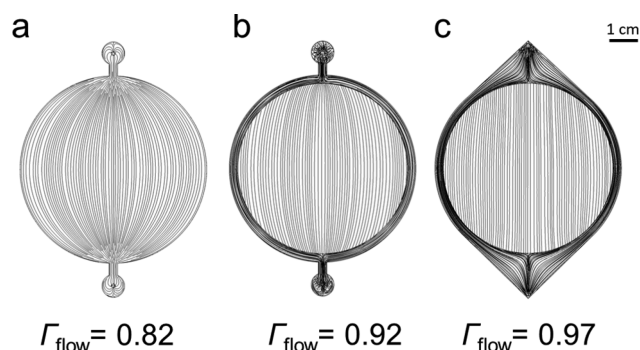


**Figure 3.** COMSOL-simulated hydrodynamic flow lines of the evolving circular FFE design: (a) a simple circular design with a constant depth of  $250 \mu\text{m}$ , (b) a device with a 3 mm-deep electrode-containing sacrificial channel around the 60 mm diameter of the separation zone, and (c) an eye-shaped device with the electrode-containing channel and deepened entrance and exit zones. The values of the corresponding uniformity index  $\Gamma_{\text{flow}}$  are shown.

in a virtual design with such features diverges from the source and converges to the sink. The flow lines are visibly curved resulting in the uniformity index  $\Gamma_{\text{flow}} = 0.82$ .

When developing rectangular CFE devices, we identified and successfully used two device features as a means of flow uniformization: (i) deep sacrificial channels around the separation zone, which also serve for placing electrodes, and (ii) deep and large entry and exit zones.<sup>18</sup> We decided to explore these two features in a circular CFE device before even looking for any other means of flow uniformization.

As in a rectangular design, adding sacrificial channels to a circular design drastically improved flow uniformity. We gradually increased the depth of the channels to reach flow uniformity of  $\Gamma_{\text{flow}} > 0.9$  (Figure 3b). We did not proceed with further depth increase as it started causing an unjustifiable decrease of the flow velocity in the separation zone. Instead, we explored adding the entrance and exit zones to the device with the channels, which proved to further increase flow uniformity. The shapes of the zones were varied to achieve the maximum value of  $\Gamma_{\text{flow}} = 0.97$  with an eye-shaped device (Figure 3c). Notably, this flow uniformity in a circular device was higher than in the best rectangular device previously assessed ( $\Gamma_{\text{flow}} = 0.95$ ) and allowed us not to look for any other means of flow uniformization. While the reason for better flow uniformity in a circular device was not further investigated, we attribute this fact to the absence of flow-disturbing corners in the circular device. Solving the flow uniformity issue allowed us to concentrate on electric field uniformity in the eye-shaped device (Figure 3c).

We chose segmented arced electrodes with segments spaced by a short distance from each other and occupying the entire perimeter of the separation zone (Figure 4). Several segments

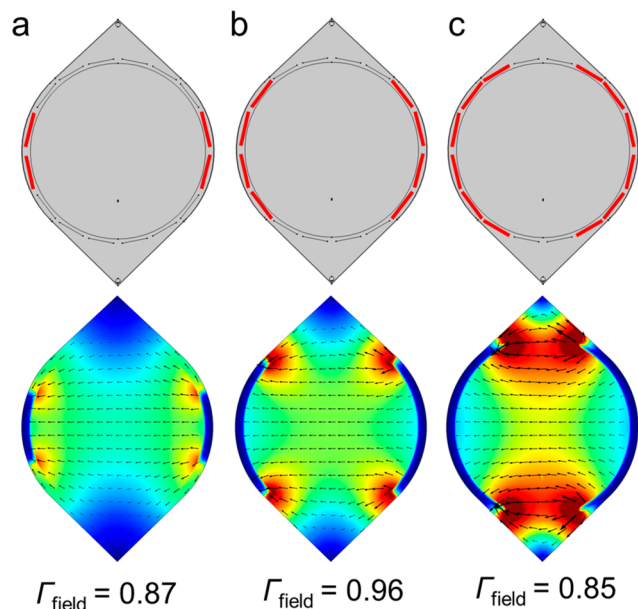


**Figure 4.** Influence of the electrode length on the uniformity of electric field in the eye-shaped CFE device with 16 electrode segments in total with (a) two, (b) four, and (c) six segments per each electrode. The top panel depicts electrode segmentation; active segments are shown in red. The bottom panel shows COMSOL-simulated electric field vectors.

would be connected to each other to form each of the two electrodes on the opposite sides of the separation zone. A voltage would be applied to these electrodes to create an electric field in the separation zone. We varied (i) the total number of segments and (ii) the length of electrodes (the number of segments per electrode) in our virtual instrument to assess their influence on field uniformity.

Three total numbers of electrode segments were considered: 24, 20, and 16. The total lengths of the electrodes were kept approximately constant by activating approximately half of the segments. This varying segmentation had a negligible effect on the field uniformity; the index of uniformity was  $\Gamma_{\text{field}} \approx 0.96$  for all three cases (Figure S2) allowing us to choose either number of segments. To decide between 24, 20, and 16, we used a practical consideration. In theory, a large number of segments provides a high degree of flexibility for setting the direction and magnitude of the electric field. However, in practice, a larger number of segments creates a greater engineering challenge. Accordingly, we chose 16 segments for our evolving functional circular CFE device.

We then varied the lengths of electrodes by changing the number of segments per electrode from two to six (Figure 4). Increasing the electrode length increases the surface area of the electrode, which, in turn, would increase the electric current in a real CFE device. Since high currents are undesirable in electrophoresis (due to Joule heating and bubble generation, for example), we aimed to find the minimum length needed for field uniformity of  $\Gamma_{\text{field}} \geq 0.95$  in the separation zone. We found that four segments per electrode (Figure 4b) resulted in  $\Gamma_{\text{field}} = 0.96$  and, thus, satisfied our criterion. Accordingly, this

electrode length was used in our further *in silico* and experimental studies.

The above-described COMSOL simulation proved that our circular CFE device could support both a uniform hydrodynamic flow ( $\Gamma_{\text{flow}} = 0.97$ ) and a uniform electric field ( $\Gamma_{\text{field}} = 0.96$ ). It is instructive to compare the overall field-flow uniformity of a circular CFE device to that of a rectangular CFE device (Figure 5). The shaded areas ( $16 \text{ cm}^2$ ) indicate

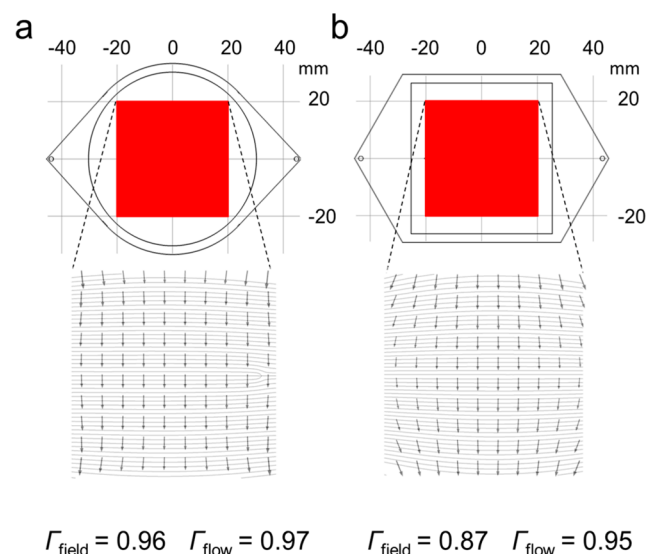


**Figure 5.** Comparison of field-flow uniformity of (a) circular CFE to that of (b) rectangular CFE. The top panels show general geometries of the respective devices, and the bottom panels show COMSOL-simulated overlaid flow lines and field vectors in these devices. The red  $40 \text{ mm} \times 40 \text{ mm}$  area is where the uniformity index for the circular device is greater than 0.95 for both field and flow. The uniformity indexes within the same square within the rectangular device were lower. The bottom images show flow lines and field vectors.

parts of the separation zones in which both the flow and field are uniform with  $\Gamma_{\text{field}} > 0.95$ . Those parts have similar sizes relative to the total area of separation zones: 57% for the circular device and 64% for the rectangular device. This comparison clearly shows that the overall field-flow uniformity of a CFE device is not compromised when the device's rotational symmetry changes from the second order to a higher order.

We then used the circular device optimized for flow and field uniformity to simulate the separation of three analytes: two with negative electrophoretic mobilities and one with zero mobility. The chosen electrode design with 16 segments in total and four segments per electrode allows eight different field-to-flow angles from  $0^\circ$  to  $157.5^\circ$ , with a step of  $22.5^\circ$ . Each of them was used to investigate the influence of the angle on CFE separation. The streams for eight angles are shown in Figure 6a, while the corresponding angulagrams can be found in Figure S3. The angular resolution was calculated from the angulagrams using the previously reported approach.<sup>16</sup> The resolution was found to depend on the field-to-flow-angle (Figure 6b). The maximum and minimum resolutions are achieved at angles different from  $90^\circ$ , which agrees with the theory of CFE.<sup>19</sup> The improvement in resolution is obtained only for angles greater than  $90^\circ$ .

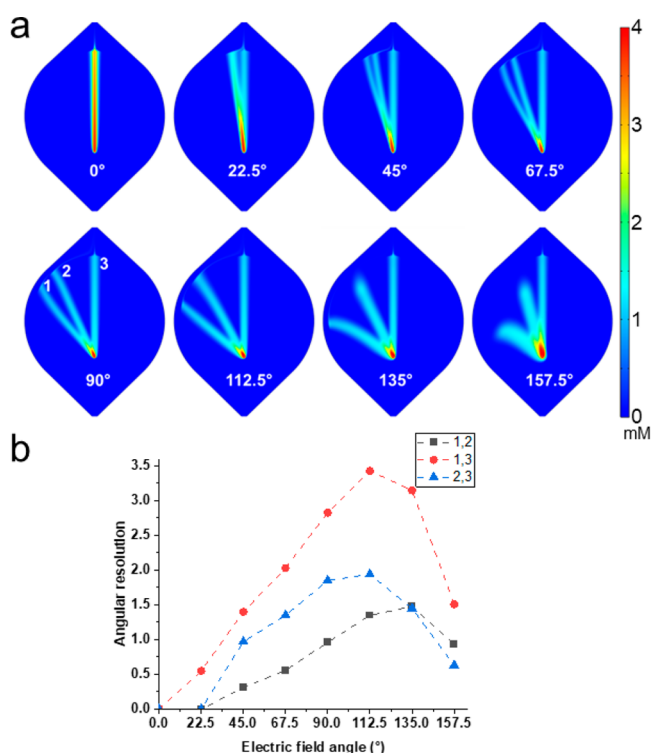


**Figure 6.** Effect of the field-to-flow angle on simulated CFE of three species with electrophoretic mobilities  $\mu_1 = -1.01 \times 10^{-8}$ ,  $\mu_2 = -5.66 \times 10^{-9}$ , and  $\mu_3 = 0$  m<sup>2</sup>/(V s). These mobilities correspond to fluorescein,  $\alpha$ -naphtholbenzein, and Sudan Black, respectively, measured in nonaqueous capillary electrophoresis as described in Note S3. Each analyte has a starting concentration of 1.25 mM. Panel a shows the separated stream at eight different angles, and panel b shows the dependence of the angular resolution (calculated from the streams in panel a via intermediate angulagrams) on the field-to-flow angle. The volumetric flow rate and electric field strength were typical for real CFE experiments in a device of this scale: 2 mL/min and 25 V/cm, respectively.

Overall, our COMSOL investigation of circular CFE proved its feasibility and provided a preoptimized design for further fabrication and evaluation of the circular CFE device. No optimization of real CFE devices was necessary. The circular device was fabricated using the same Solid Edge code as the one used for creating device geometry in COMSOL. Using the same code ensured that the physical device was identical to the virtual device within the precision of our fabrication process. The details of the fabrication steps are described in Note S4, while experimental details on CFE can be found in Note S5.

Flow uniformity in the physical CFE device was tested by flowing fluorescent beads added to the background electrolyte through the device at a zero electric-field strength. Figure 7a demonstrates an image with flow lines derived from a video of fluorescence from the moving beads (Video S1). The video was used to create a vector field (Figure 7b) using Fiji/TrackMate,<sup>20–22</sup> which, in turn, was utilized to calculate flow uniformity index  $\Gamma_{\text{flow}} \approx 0.91$  (Note S6). This value is similar to that predicted in COMSOL, providing cross-validation for COMSOL modeling and experiments in a physical device.

We did not have a direct way of investigating electric field uniformity. Therefore, we assessed it via evaluating stream linearity in CFE separation; if the electric field is nonuniform, then streams are nonlinear even if the flow is uniform. We run the separation of four species and found that stream linearity

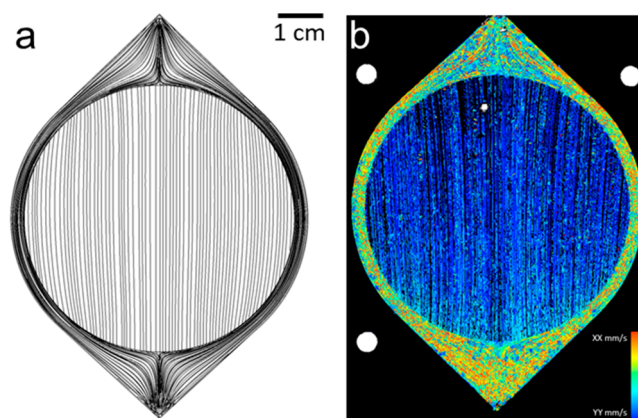


**Figure 7.** Assessment of flow uniformity in circular CFE via flowing fluorescent beads through the device without electric field and with an average flow velocity of 0.09 mm/s in the separation zone. Panel a shows the flow field produced by COMSOL software. Panel b shows the vector field produced from the video with Fiji/TrackMate and used to calculate uniformity index  $\Gamma_{\text{flow}} = 0.91$ .

was  $\geq 0.95$  for all four streams (Figure 8a). The results of these experiments indirectly proved that the electric field was uniform in a circular CFE device.

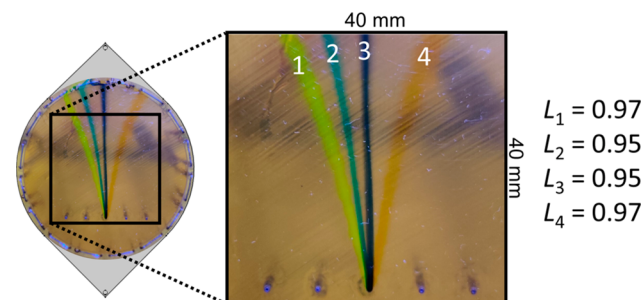


**Figure 8.** Indirect assessment of electric-field uniformity in a circular CFE device via evaluation of stream linearity of fluorescein (stream 1),  $\alpha$ -naphtholbenzein (stream 2), Sudan Black B (stream 3), and DMAS (stream 4). The field-to-flow angle was 90°. Experimental details can be found in Note S5. Stream linearities are shown to the right of the image.

Proving that the real circular CFE device supports uniform flow and field allowed us to move to the ultimate goal of this study: an experiment assessing the influence of the field-to-flow orientation on CFE. We used three analytes: negatively charged fluorescein, negatively charged  $\alpha$ -naphtholbenzein, and neutral Sudan Black. Note that their mobilities were utilized in simulated CFE shown in Figure 4, and 112.5° was an angle for the best resolution of both fluorescein and  $\alpha$ -naphtholbenzein from Sudan Black. Accordingly, in our CFE experiments separation quality was compared at two field-to-flow angles, i.e., 90° and 112.5° (Figure 9). The dependence of stream deflection on the angle was in a manner predicted in both COMSOL modeling and in the theory of CFE. Stream resolution was significantly higher for 112.5° than for 90°. These experiments provided the final proof-of-concept for circular CFE.

While the results of experiments correspond qualitatively to those of the in silica study, there is a significant quantitative disagreement. The two major potential reasons for this disagreement are (i) experimental imperfections (e.g.,

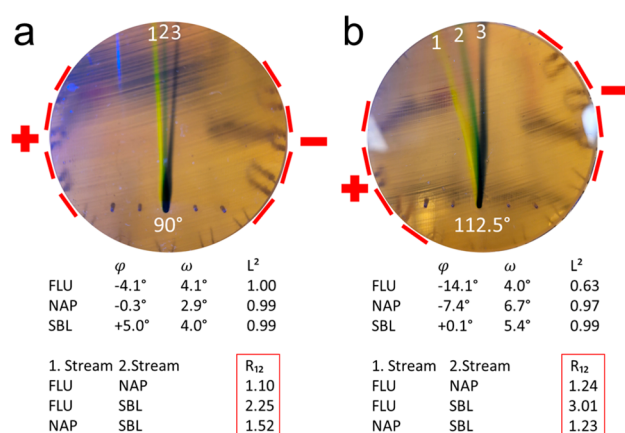


**Figure 9.** Comparison of CFE of fluorescein (FLU, stream 1),  $\alpha$ -naphtholbenzenol (NAP, stream 2), and Sudan Black (SBL, stream 3) with 90° (a) and 112.5° (b) field-to-flow angle at an electric field of 25 V/cm and a flow rate of 4 mL/min.

inaccurately measured values of electrophoretic mobilities of the two charged species) and (ii) secondary phenomena, which were present in the experiment but not included in COMSOL simulation. The second reason is more interesting as it can potentially reveal a phenomenon that has been previously disregarded by CFE practitioners. A known secondary phenomenon is the electroosmotic flow (EOF), which is very common in aqueous electrophoresis<sup>23,24</sup> and can also be beneficial.<sup>25,26</sup> However, here we used nonaqueous CFE in which EOF is negligible, which was confirmed by no deflection of the stream of the electrically neutral analyte. Therefore, we looked for another reason.

While using the field-to-flow angles different from 90°, we noticed a decrease in the flow velocity in the separation zone, which could be seen by following stream evolution for the neutral molecule. We hypothesized that this flow slowing was caused by ion concentration polarization. The phenomenon of ion concentration polarization is well known in the area of ion transport but has never been mentioned in the context of CFE; the reader is referred to multiple other publications for details.<sup>27–30</sup> This phenomenon is caused by the ion concentration gradient and is accompanied by recirculation of the flow near the electrodes. To check if the recirculation was detectable, we followed the flow pattern near the electrodes with fluorescent beads added to the background electrolyte. We found profound flow recirculation (Video S2), which confirms that ion concentration polarization is always present in CFE but does not have the same magnitude when electrodes are not segmented or in hydrodynamic flows with high Peclet numbers. This phenomenon can also explain the curving of the streams at angles other than 90°. While it would be interesting to include it in our simulation of CFE to see if this could improve quantitative agreement with the experiment, COMSOL does not have suitable capabilities. We did not find in our experimental results any signs of other phenomena that could contribute to the quantitative disagreement.

In summary, we proposed the concept and proved the feasibility of high-order symmetry in MSS. It was implemented in a working proof-of-concept CFE device with a circular separation zone and arc-shaped electrodes positioned in a deep channel surrounding the separation zone. This circular CFE can support flow and electric-field uniformity on par with or

higher than those of canonic rectangular CFE. Both simulations and experiments confirmed the theoretical prediction that the best stream resolution is achieved at a field-to-flow angle different from 90°. Some quantitative disagreements between the results of simulation and experiments prompted us to look for secondary phenomena unaccounted in simulation. We identified one such phenomenon: ion concentration polarization. This phenomenon does not clearly manifest itself unless the field-to-flow angle is varied or the flow pattern near the electrodes is analyzed in detail. Accordingly, it is the first time when ion concentration polarization is reported in the context of CFE. We foresee that circular CFE will serve as a testbed for the investigation and creation of new CFE modalities. It is instructive to mention that the idea of circular CFE was conceived by recent advances in presenting CFE in polar rather than a Cartesian system of coordinates.

To conclude, we would like to emphasize that the fabrication process of circular and rectangular devices is the same; the circular CFE device in this work was created using our previously developed manufacturing process avoiding addition of extra complexity and maintaining feasibility (Note S7). In contrast to rectangular CFE, circular CFE provides three important advantages: (1) It is better aligned with the polar nature of CFE. (2) It provides better field and flow homogeneity. (3) It can provide improved resolution when utilized with nonorthogonal field-to-flow orientation (the gain in resolution is theoretically limited to several folds at most for all typical analytes). We see no advantages of rectangular CFE and recommend the use of circular one by default.

## ■ ASSOCIATED CONTENT

### Supporting Information

The Supporting Information is available free of charge at <https://pubs.acs.org/doi/10.1021/acs.analchem.2c01829>.

List of supporting files deposited on ChemRxiv, CAC geometry transformation (Figure S1), varying the total number of electrode segments (Figure S2), angulagrams for Figure 6a (Figure S3), Index of Uniformity calculations (Note S1), list of COMSOL models (Note S2), measurements of electrophoretic mobilities in CE (Note S3), circular CFE device fabrication details (Note S4), circular CFE experimental details (Note S5), using Fiji/TrackMate for the circular design flow field  $\Gamma$  calculations (Note S6), and fabrication timeline for rectangular and circular devices (Note S7) (PDF)

Video S1: Fluorescent beads time lapse for flow field  $\Gamma$  calculations in Note S6 (MOV)

Video S2: Flow vortexing due to ion concentration polarization (MP4)

## ■ AUTHOR INFORMATION

### Corresponding Author

Sergey N. Krylov – Department of Chemistry and Centre for Research on Biomolecular Interactions, York University, Toronto, Ontario M3J 1P3, Canada; [orcid.org/0000-0003-3270-2130](https://orcid.org/0000-0003-3270-2130); Email: [skrylov@yorku.ca](mailto:skrylov@yorku.ca)

### Authors

Sven Kochmann – Department of Chemistry and Centre for Research on Biomolecular Interactions, York University,

Toronto, Ontario M3J 1P3, Canada; Present Address: S. Kochmann: Department of Chemistry, Institute of Analytical Chemistry, University of Natural Resources and Life Sciences, Muthgasse 18, 1190 Vienna, Austria; [orcid.org/0000-0001-7423-4609](https://orcid.org/0000-0001-7423-4609)

Nikita A. Ivanov – Department of Chemistry and Centre for Research on Biomolecular Interactions, York University, Toronto, Ontario M3J 1P3, Canada; [orcid.org/0000-0002-0842-6626](https://orcid.org/0000-0002-0842-6626)

J. C. Yves Le Blanc – SCIEX, Concord, Ontario L4K 4 V8, Canada

Boris I. Gorin – Eurofins CDMO Alphora, Mississauga, Ontario L5K 1B3, Canada; [orcid.org/0000-0003-1500-5392](https://orcid.org/0000-0003-1500-5392)

Complete contact information is available at:

<https://pubs.acs.org/10.1021/acs.analchem.2c01829>

### Author Contributions

<sup>†</sup>S. Kochmann and N. A. Ivanov contributed equally.

### Author Contributions

The manuscript was written through contributions of all authors. All authors have given approval to the final version of the manuscript.

### Notes

The authors declare no competing financial interest.

## ACKNOWLEDGMENTS

This work was supported by the NSERC grant (STPG-P 521331-2018) to S.N.K.

## ABBREVIATIONS

MSS, molecular stream separation; CFE, continuous-flow electrophoresis; CAC, continuous annular chromatography; TLC, thin layer chromatography;  $\Gamma$ , index of uniformity; FLU, fluorescein; NAP,  $\alpha$ -naphtholbenzyl; SBL, Sudan black B; DMAS, 2-[4-(dimethylamino)styryl]-1-methylpyridinium iodide; EOF, electroosmotic flow

## REFERENCES

- (1) Bloemendal, V. R. L. J.; Janssen, M. A. C. H.; van Hest, J. C. M.; Rutjes, F. P. J. T. *React. Chem. Eng.* **2020**, *5* (7), 1186–1197.
- (2) Espro, C.; Rodríguez-Padrón, D. *Curr. Opin. Green Sustain. Chem.* **2021**, *30*, 100478.
- (3) Gioiello, A.; Piccinno, A.; Lozza, A. M.; Cerra, B. *J. Med. Chem.* **2020**, *63* (13), 6624–6647.
- (4) Britton, J.; Raston, C. L. *Chem. Soc. Rev.* **2017**, *46* (5), 1250–1271.
- (5) Jiao, J.; Nie, W.; Yu, T.; Yang, F.; Zhang, Q.; Aihemaiti, F.; Yang, T.; Liu, X.; Wang, J.; Li, P. *Chem. – Eur. J.* **2021**, *27* (15), 4817–4838.
- (6) Pfeiffer, S. A.; Rudisch, B. M.; Glaeser, P.; Spanka, M.; Nitschke, F.; Robitzki, A. A.; Schneider, C.; Nagl, S.; Belder, D. *Anal. Bioanal. Chem.* **2018**, *410* (3), 853–862.
- (7) Liu, Y.; Chen, G.; Yue, J. *J. Flow Chem.* **2020**, *10* (1), 103–121.
- (8) Kralj, J. G.; Sahoo, H. R.; Jensen, K. F. *Lab Chip* **2007**, *7* (2), 256–263.
- (9) Rudisch, B. M.; Pfeiffer, S. A.; Geissler, D.; Speckmeier, E.; Robitzki, A. A.; Zeitler, K.; Belder, D. *Anal. Chem.* **2019**, *91* (10), 6689–6694.
- (10) Ivanov, N. A.; Liu, Y.; Kochmann, S.; Krylov, S. N. *Lab. Chip* **2019**, *19* (13), 2156–2160.
- (11) Zhou, L.; Wu, K.; Qin, W.; Wang, G.; Fu, D.; Fei, W. *Sci. China Chem.* **2015**, *58* (7), 1187–1192.

(12) Turgeon, R. T.; Bowser, M. T. *Anal. Bioanal. Chem.* **2009**, *394* (1), 187–198.

(13) Evenhuis, C. J.; Okhonin, V.; Krylov, S. N. *Anal. Chim. Acta* **2010**, *674* (1), 102–109.

(14) Pamme, N. *Lab. Chip* **2007**, *7* (12), 1644.

(15) Rathore, A. S.; Kumar, D.; Kateja, N. *Biotechnol. Lett.* **2018**, *40* (6), 895–905.

(16) Kochmann, S.; Krylov, S. N. *Anal. Chem.* **2018**, *90* (15), 9504–9509.

(17) Agostino, F. J.; Evenhuis, C. J.; Krylov, S. N. *J. Sep. Sci.* **2011**, *34* (5), 556–564.

(18) Agostino, F. J.; Cherney, L. T.; Galievsky, V.; Krylov, S. N. *Angew. Chem., Int. Ed.* **2013**, *52* (28), 7256–7260.

(19) Okhonin, V.; Evenhuis, C. J.; Krylov, S. N. *Anal. Chem.* **2010**, *82* (4), 1183–1185.

(20) Schindelin, J.; Arganda-Carreras, I.; Frise, E.; Kaynig, V.; Longair, M.; Pietzsch, T.; Preibisch, S.; Rueden, C.; Saalfeld, S.; Schmid, B.; Tinevez, J.-Y.; White, D. J.; Hartenstein, V.; Eliceiri, K.; Tomancak, P.; Cardona, A. *Nat. Methods* **2012**, *9* (7), 676–682.

(21) Tinevez, J.-Y.; Perry, N.; Schindelin, J.; Hoopes, G. M.; Reynolds, G. D.; Laplantine, E.; Bednarek, S. Y.; Shorte, S. L.; Eliceiri, K. W. *Methods* **2017**, *115*, 80–90.

(22) Ershov, D.; Phan, M.-S.; Pylvänäinen, J. W.; Rigaud, S. U.; Le Blanc, L.; Charles-Orszag, A.; Conway, J. R. W.; Laine, R. F.; Roy, N. H.; Bonazzi, D.; Duménil, G.; Jacquemet, G.; Tinevez, J.-Y. Bringing TrackMate into the Era of Machine-Learning and Deep-Learning. *bioRxiv Preprint*, 2021. DOI: 10.1101/2021.09.03.458852.

(23) Fonslow, B. R.; Bowser, M. T. *Anal. Chem.* **2006**, *78* (24), 8236–8244.

(24) Mesbah, K.; Mai, T. D.; Jensen, T. G.; Sola, L.; Chiari, M.; Kutter, J. P.; Taverna, M. *Microchim. Acta* **2016**, *183* (7), 2111–2121.

(25) Bacheva, V.; Paratore, F.; Rubin, S.; Kaigala, G. V.; Bercovici, M. *Angew. Chem., Int. Ed.* **2020**, *59* (31), 12894–12899.

(26) Rosenfeld, T.; Bercovici, M. *Lab. Chip* **2019**, *19* (2), 328–334.

(27) de Valença, J. C.; Wagterveld, R. M.; Lammertink, R. G. H.; Tsai, P. A. *Phys. Rev. E* **2015**, *92* (3), 031003.

(28) Hanasoge, S.; Diez, F. J. *Lab. Chip* **2015**, *15* (17), 3549–3555.

(29) Liu, W.; Ren, Y.; Xue, R.; Song, C.; Wu, Q. *ELECTROPHORESIS* **2020**, *41* (10–11), 778–792.

(30) Liu, W.; Ren, Y.; Tao, Y.; Zhou, Z.; Wu, Q.; Xue, R.; Yao, B. *J. Phys. Appl. Phys.* **2020**, *53* (17), 175304.

# Supporting Information

## Circular Geometry in Molecular Stream Separation to Facilitate Non-Orthogonal Field-to-Flow Orientation

Sven Kochmann,<sup>‡1,2</sup> Nikita A. Ivanov,<sup>‡1</sup> J. C. Yves Le Blanc,<sup>3</sup> Boris I. Gorin,<sup>4</sup> and Sergey N. Krylov<sup>\*1</sup>

<sup>1</sup>Department of Chemistry and Centre for Research on Biomolecular Interactions, York University  
4700 Keele Street, Toronto, Ontario M3J 1P3, Canada

<sup>2</sup>Current address: Department of Chemistry, Institute of Analytical Chemistry, University of Natural Resources and Life Sciences, Muthgasse 18, 1190 Vienna, Austria

<sup>3</sup>SCIEX, 71 Four Valley Drive, Concord, Ontario L4K 4V8, Canada

<sup>4</sup>Eurofins CDMO Alphora, 2395 Speakman Drive #2001, Mississauga, Ontario L5K 1B3, Canada

**Abstract:** Molecular stream separation (MSS) is a promising complement for continuous-flow synthesis. MSS is driven by forces exerted on molecules by a field applied at an angle to the stream-carrying flow. MSS has only been performed with a 90° field-to-flow angle because of a rectangular geometry of canonic MSS; the second-order rotational symmetry of a rectangle prevents any other angle. Here, we propose a non-canonic circular geometry for MSS, which better aligns with the polar nature of MSS and allows changing the field-to-flow. We conducted *in silico* and experimental studies of circular geometry for continuous-flow electrophoresis (CFE, an MSS method). We proved two advantages of circular CFE over its rectangular counterpart. First, circular CFE can support better flow and electric-field uniformity than rectangular CFE. Second, the non-orthogonal field-to-flow orientation, achievable in circular CFE, can result in a higher stream resolution than the orthogonal one. Considering that circular CFE devices are not more complex in fabrication than rectangular ones, we foresee that circular CFE will serve as a new standard and a testbed for the investigation and creation of new CFE modalities.

## Table of Contents

	Page
Figure S1. CAC geometry transformation . . . . .	S3
Figure S2. Varying the total number of the electrode segments . . . . .	S4
Figure S3. Angulagrams for Figure 6a . . . . .	S5
Note S1. Index of Uniformity calculations . . . . .	S6
Note S2. List of COMSOL models . . . . .	S8
Note S3. Measurements of electrophoretic mobilities in CE . . . . .	S9
Note S4. Circular CFE device fabrication details . . . . .	S10
Note S5. Circular CFE experimental details . . . . .	S11
Note S6. Using Fiji/TrackMate for the circular design flow field $\Gamma$ calculations . . . . .	S12
Note S7. Fabrication timeline for rectangular and circular devices. . . . .	S14
Supporting References . . . . .	S15
Author Contributions . . . . .	S15

This manuscript is accompanied by other supporting files:

Note S2 files. COMSOL models (.mph files), check page S8 for the complete list of models.

Note S6 files. Fiji/TrackMate Evaluation files, check page S13 for the method.

Video S1. Fluorescent beads time-lapse for flow field  $\Gamma$  calculations in Note S6.

Video S2. Flow vortexing flow due to Ion Concentration polarisation.

These files are also available in the preprint version of this manuscript at ChemRxiv:  
<https://chemrxiv.org/engage/chemrxiv/article-details/623af6a3658bc0fb97b5146c>  
DOI: 10.26434/chemrxiv-2022-3w7gt

**Figure S1. CAC geometry transformation**

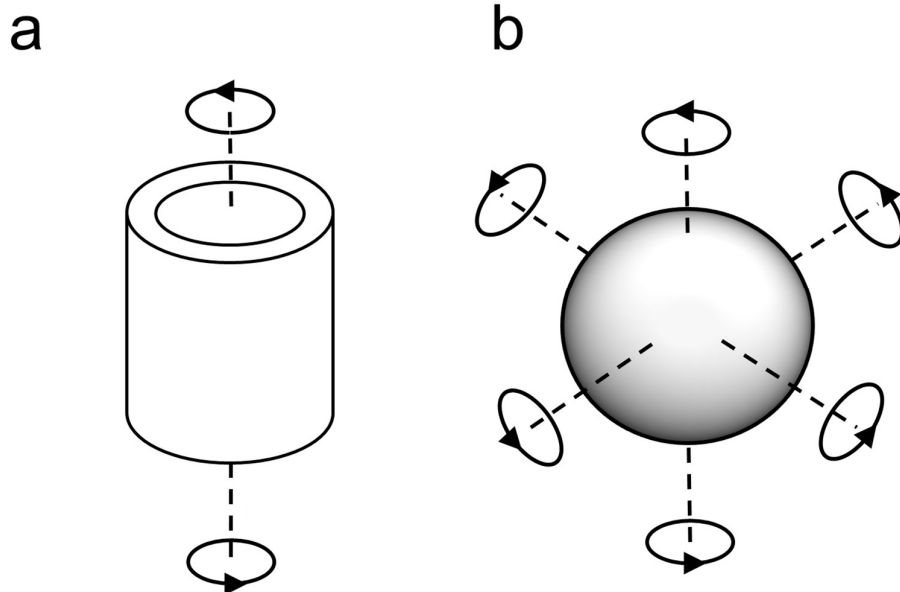


**Figure S1.** Illustration of **a)** conventional CAC geometry with one infinite rotation axis at the center of the cylinder and **b)** transformed geometry that contains additional infinite rotational axis orthogonal to the surface of the sphere.

**Figure S2. Varying the total number of the electrode segments**

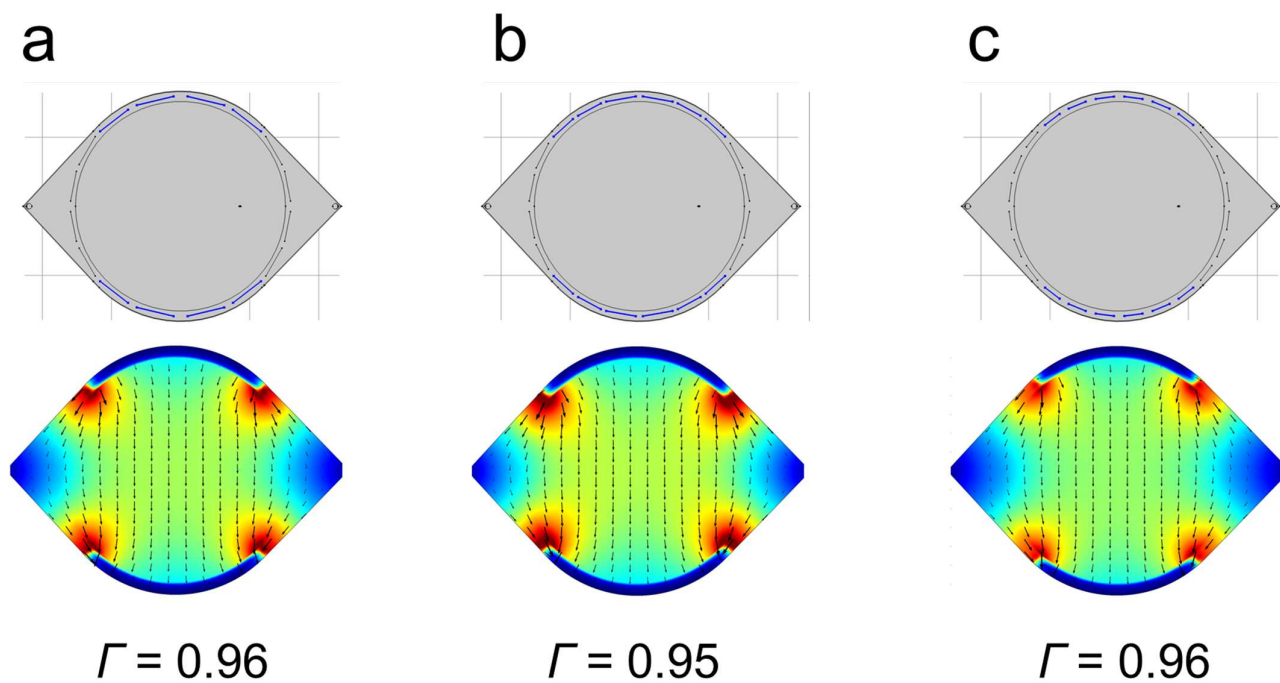


**Figure S2.** Illustration of potential geometries containing **a)** 16, **b)** 20, and **c)** 24 electrodes and their corresponding COMSOL simulated electric fields.

**Figure S3. Angulagrams for Figure 6a**

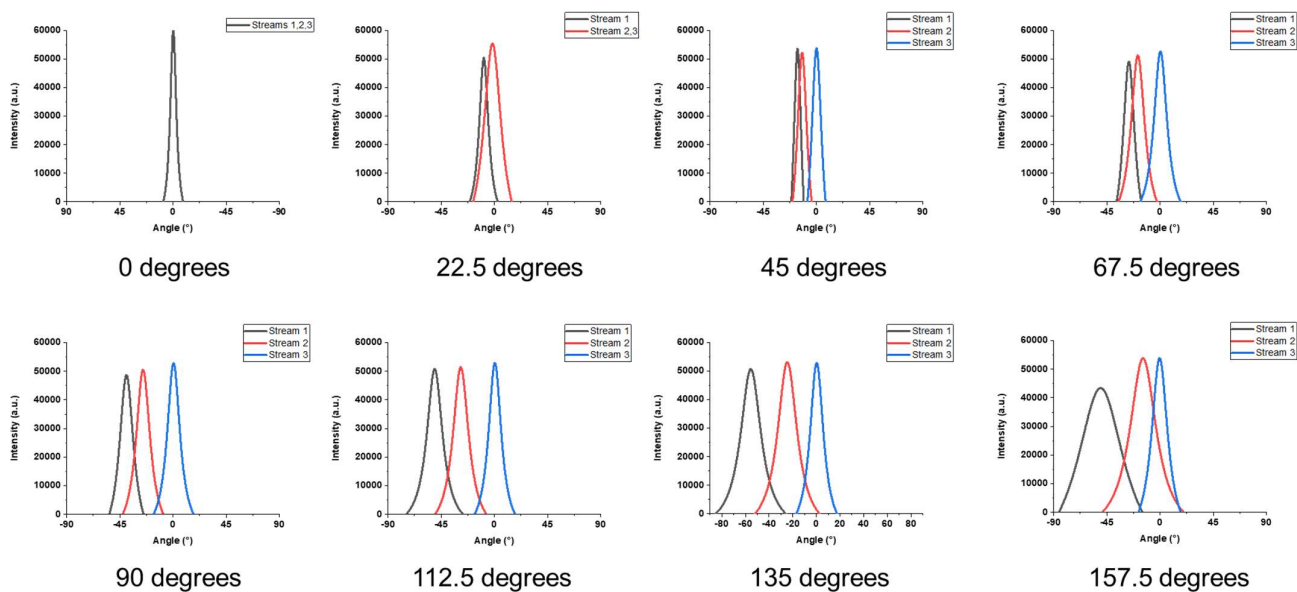


**Figure S3.** Angulagrams for molecular streams in Figure 6a in the main text. The angulagrams were generated using Topino software.<sup>1</sup>

### Note S1. Index of Uniformity calculations

A two-dimensional vector field is exported as a four-column data set consisting of two-number coordinates and corresponding X,Y vector components. The sum of all X vector components and the sum of all Y vector components are used to find the average flow vector for the entire device (Eq.1). This average vector points in the general direction of the flow within the device.

$$\text{Average flow vector} = \left( \sum X_{\text{components}}, \sum Y_{\text{components}} \right) \quad (1)$$

The angle  $\varphi$  from Eq. 2, calculates the angular deflection of the average vector from the X-axis.

$$\varphi = -\arctan\left(\frac{\sum Y_{\text{components}}}{\sum X_{\text{components}}}\right) \quad (2)$$

This angle is then used to rotate the entire vector field using Eq. 3 and Eq. 4 along the X-axis for further calculations.  $X'$  and  $Y'$  are the newly obtained vector components after the rotation:

$$X' = X_{\text{component}} \cos \varphi - Y_{\text{component}} \sin \varphi \quad (3)$$

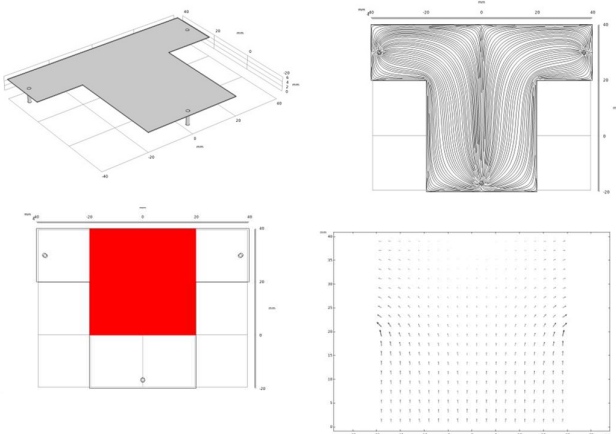
$$Y' = X_{\text{component}} \sin \varphi - Y_{\text{component}} \cos \varphi \quad (4)$$

The homogeneity factor ( $\Gamma$ ) is then calculated as in Eq. 5. In any real device, rotation of the general flow direction in the direction of the X axis, allows the ratio component of Eq. 5 to always be between 0 and 1. In the ideal case of a perfect homogenous flow,  $\Gamma$  will be equal to 1. All flow non-homogeneities would increase the  $|Y'_{\text{components}}|$  part and decrease the  $\Gamma$  value.

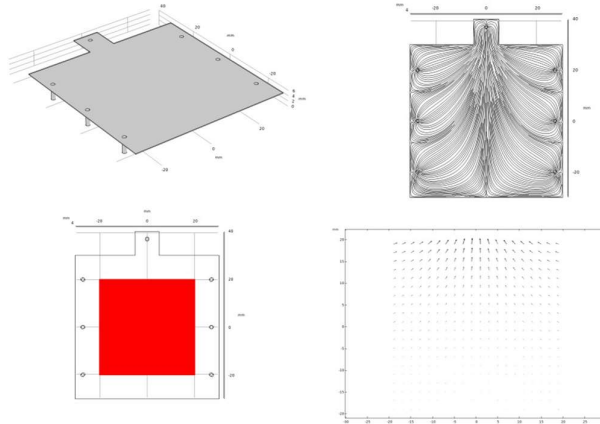
$$\Gamma = 1 - \frac{\sum |Y'_{\text{components}}|}{\sum |X'_{\text{components}}|} \quad (5)$$

Example of  $\Gamma$  values for different geometries are shown below.

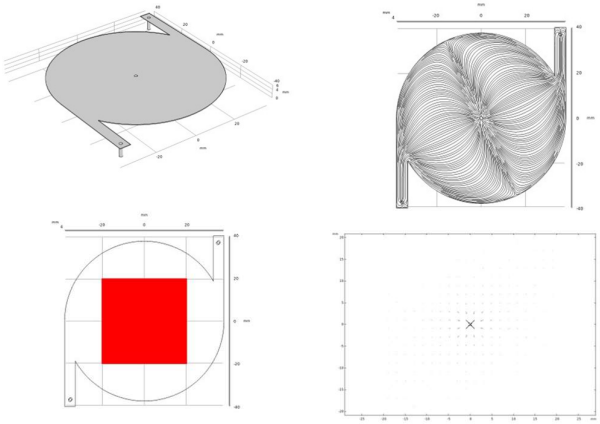
Examples of  $\Gamma$  for different geometries with non-homogenous flow



$\Gamma = 0.631$



$\Gamma = 0.311$



$\Gamma = 0.282$

## Note S2. List of COMSOL models included in the supporting information

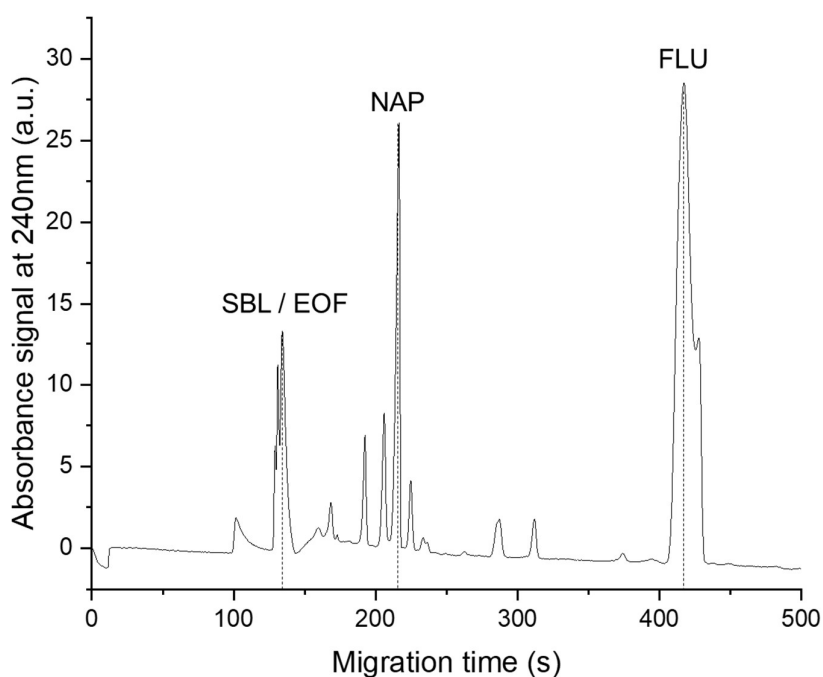
The complete list of COMSOL models (.mph) deposited into ChemRxiv:

1. Circular device geometry evolution models (Figure 3)
  - 1.1. Circle prototype 250 micron uniform thickness (Figure 3a)
  - 1.2. Circle prototype 3mm electrode channels (Figure 3b)
  - 1.3. "The eye" 3mm electrode channels (Figure 3c)
  
2. Examples of  $\Gamma$  for non-ideal flow geometries (Note S1 Continued, page S7)
  - 2.1. T splitter geometry flow field
  - 2.2. Square multiple inlets flow field
  - 2.3. Sink with 2 inlets flow field
  
3. Varying the total number of electrodes in the circular device (Figure S2, page S4)
  - 3.1. 16 segments with 8 active electrodes (Figure S2a)
  - 3.2. 20 segments with 12 active electrodes (Figure S2b)
  - 3.3. 24 segments with 12 active electrodes (Figure S2c)
  
4. Varying the number of active electrodes in the circular device (Figure 4)
  - 4.1. 16 segments with 4 active electrodes (Figure 4a)
  - 4.2. 16 segments with 8 active electrodes (Figure 4b)
  - 4.3. 16 segments with 12 active electrodes (Figure 4c)
  
5. Varying the angle in non-orthogonal separation models (Figure 6)
  - 5.1. 16 segments with 8 active electrodes, 0 degrees between flow and electric field
  - 5.2. 16 segments with 8 active electrodes, 22.5 degrees between flow and electric field
  - 5.3. 16 segments with 8 active electrodes, 45 degrees between flow and electric field
  - 5.4. 16 segments with 8 active electrodes, 67.5 degrees between flow and electric field
  - 5.5. 16 segments with 8 active electrodes, 90 degrees(orthogonal) between flow and electric field
  - 5.6. 16 segments with 8 active electrodes, 112.5 degrees between flow and electric field
  - 5.7. 16 segments with 8 active electrodes, 135 degrees between flow and electric field
  - 5.8. 16 segments with 8 active electrodes, 157.5 degrees between flow and electric field

### Note S3. Measurements of electrophoretic mobilities in CE

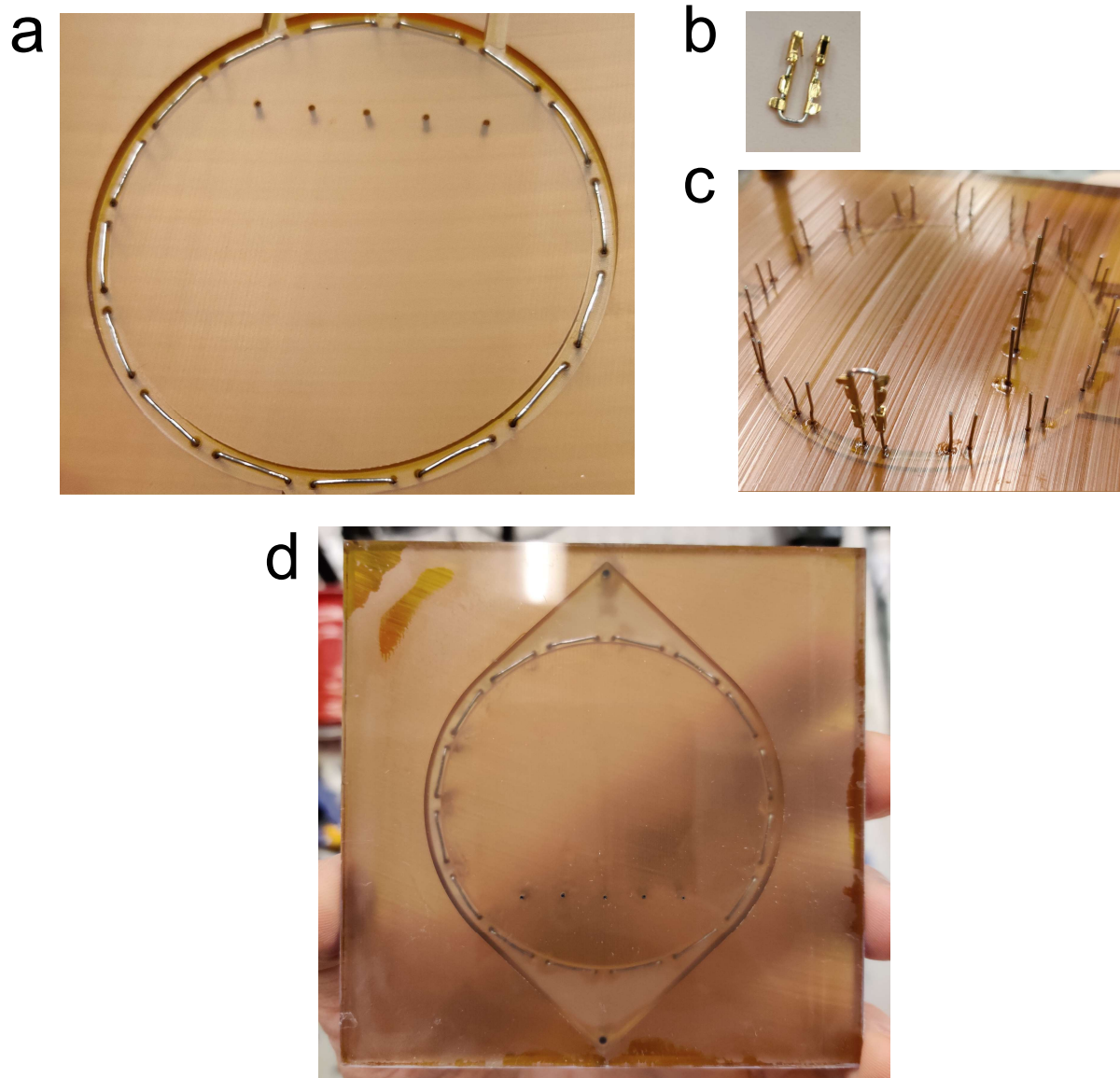
All CE experiments were done with a P/ACE MDQ instrument from Sciex (Concord, ON, Canada). Light absorption at 240 nm was used for analyte detection using the direct absorbance method. An uncoated fused silica capillary with an inner diameter of 75  $\mu\text{m}$ , total length of 30 cm, and distance from the inlet to the detection point of 20 cm was used for all CE experiments when measuring  $\mu$  (electrophoretic mobility) of fluorescein (FLU), Sudan Black (SBL) and  $\alpha$ -naphtholbenzein (NAP). The background electrolyte was 30 mM tetrabutylammonium acetate (TBAA) in propylene carbonate. An EOF marker (1.0 mM toluene dissolved in the background electrolyte) was injected along with 1 mM of each analyte into the anode end of the capillary by a pressure pulse of 0.4 psi during 2.5 s. CE separation was carried out at an electric field of 1000 V/cm (30 kV across 30 cm) with a capillary temperature set to 25°C. Analyte migration velocities (m/s) were calculated from the corresponding electropherograms based on characteristic times required for the analyte to reach the UV detector. Experimental electrophoretic mobilities ( $\text{m}^2/(\text{Vs})$ ) were calculated by dividing experimental analyte velocities (m/s) by the applied electric field (V/m).

Analyte	Charge	Migration time, s	Migration velocity, m/s	Difference between migration velocities of the analyte and EOF, m/s	Electrophoretic mobility, $\text{m}^2/(\text{Vs})$
Toluene (EOF marker)	Neutral	133.8	0.00149	0	0
SBL	Near Neutral	133.8	0.00149	0	0
NAP	Negative	215.4	0.00092	-0.00057	$-5.7 \times 10^{-9}$
FLU	Negative	417	0.00048	-0.00101	$-1.0 \times 10^{-8}$



#### Note S4. Circular CFE device fabrication details

Circular devices were designed in Solid Edge and fabricated of PEI (polyetherimide) and PVC (polyvinylchloride) plastics according to our previously developed fabrication procedure for PMMA chips (*J. Sep. Sci.* **2011**, *34*, 556–564, DOI: 10.1002/jssc.201000758; *Lab Chip* **2017**, *17*, 256–266, DOI: 10.1039/C6LC01381C). Details on chip fabrication and chip components used (apart from the chip material) may be found in these two previous works. Circular devices were fabricated using MODELA MDX-540 Benchtop Milling Machine from Roland DGA (Irvine, CA, USA). Short  $\Pi$ -shaped palladium wires were inserted into the PEI device to create electrode segments surrounding the separation zone (**a**).  $\Pi$ -shaped nickel wires with gold-coated crimps attached on both sides (**b**) were used to connect multiple segments into a single electrode array (**c**). After electrode assembly, the PEI device was covered with a flat-machined piece of PVC plastic (**d**).



#### **Note S5. Circular CFE experimental details**

Flow rates of the background electrolyte and analyte were in the ranges of 2–4 mL/min and 1–2  $\mu\text{L}/\text{min}$ , respectively. 150 V was applied from an EPS 3501 XL power supply (GE Healthcare, Chicago, IL, USA) to the platinum electrodes around the separation zone resulting in an electric field strength of 25 V/cm (distance between the electrodes was 6 cm). Depending on the electrolyte concentration, the conductivity of our background electrolyte solution was 2 to 8  $\mu\text{S}/\text{m}$ . The electrolyte solution was delivered to the circular device with a NE-9000G peristaltic pump from New Era Pump Systems, Inc. (Farmingdale, NY, USA). The pump was equipped with a Masterflex pulse dampener from Cole Palmer (Vernon Hills, IL, USA) to suppress flow pulsation. Analyte solutions were delivered to the circular device with a Model 11 syringe pump from Harvard Apparatus (Holliston, MA, USA). A mixture of analytes (1.25 mM each; 3.75 mM combined) was prepared in the 30 mM of the electrolyte solution (exactly the same as background electrolyte) to maintain homogenous conductivity in the separation zone. Note, in Non-aqueous CFE, analytes do not have an intrinsic charge and, accordingly, do not change the overall conductivity. The analytes acquire electrophoretic mobility through their association with the background electrolyte.

## Note S6. Using Fiji/TrackMate for the circular design flow field $\Gamma$ calculations

The recorded video **flowstream.mp4** (about 13.4 GB) was edited in the following way using **ffmpeg 3.4.8** software to remove background, improve particle tracking conditions, and significantly reduce file size while maintaining high resolution:

```
# Remove audio from video
ffmpeg -i flowstream.mp4 -c copy -an flowstream_noaudio.mp4

# Remove color (reduces file size to 1/3)
ffmpeg -i flowstream_noaudio.mp4 -vf format=gray flowstream_noaudio_gray.mp4

# Cut the first 5 seconds (shaking camera)
ffmpeg -i flowstream_noaudio_gray.mp4 -ss 5 -c copy flowstream_noaudio_gray_cut.mp4

# Add overlay (removes all the chip background)
ffmpeg -i flowstream_noaudio_gray_cut.mp4 -i flowstream_overlay.png -filter_complex
"[0:v][1:v] overlay=0:0" -pix_fmt yuv420p -codec h264_nvenc
flowstream_noaudio_gray_cut_overlay.mp4

# Change curves to improve contrast
ffmpeg -i flowstream_noaudio_gray_cut_overlay.mp4 -vf "curves=all='0.04/0.0 0.08/1.0'" -
pix_fmt yuv420p -codec h264_nvenc flowstream_noaudio_gray_cut_overlay_curved.mp4

# Crop the video (removes more background, reduces the memory per frame size/requirement);
the original video is 3840x2160; also, use gray pixel format to turn everything to an
8bit image
ffmpeg -i flowstream_noaudio_gray_cut_overlay_curved.mp4 -vf "crop=1600:2160:1000:0" -
pix_fmt gray -codec h264_nvenc flowstream_noaudio_gray_cut_overlay_curved_cropped.mp4

# Create a set of tiff files with lzw compression out of this movie file; "gray" format is
important, otherwise tiffcp will not work (subsampling)
ffmpeg -i flowstream_noaudio_gray_cut_overlay_curved_cropped.mp4 -compression_algo lzw -
pix_fmt gray tiffs/flowstream%05d.tif
```

The result is a set of tiff-files, **flowstream00001.tif** to **flowstream38246.tif**, that can be used in **Fiji/ImageJ2 1.53f51** with the **TrackMate 7.6.0** plugin.<sup>2-4</sup> We found that using the video file directly or other image formats (e.g., tiff-stacks) caused importing the files to fail.

Tracking the particles in TrackMate was done by using every 10<sup>th</sup> image and selecting  $t$ -axis ("Swapping  $z$  and  $t$ "). The **Difference of Gaussian (DoG)** detector (estimated diameter: 5 px, quality threshold: 30, subpixel localization) was used for particle recognition in all images. Subsequently, all detected particles were forwarded to the **Simple Linear Assignment Problem (Simple LAP)** tracker for generating the tracks (linking max distance: 15 px; gap-closing distance: 18 px; max-frame gap: 2). The resulting information were exported to **flowstream\_tracks.xml**.

Further processing was done with developed Python scripts (see the protocol on the next page) to find the marker positions on the image (calculating the resolution and the center point), calculate, and select the flow vectors. All Python scripts can be found in the ChemRxiv depository (see page S2).

```

# Markers found using a randomly selected single image => Center point at 810, 1024;
  average distance between markers is 1408 (1415 and 1401 pixels) => 60 mm real units
  between them => 0.0426 mm/pixel
findmarkers.py --area 3600 --markers 3 --showimage flowstream01694.tif

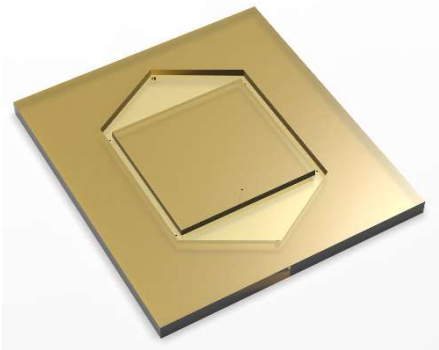
# Calculate velocity vectors; removing zero-length vectors (usually artifacts from
  tracking); removing tracks with small number of points (everything below 10); average
  the track data for one vector (reduces the impact of high errors in track
# detection between two time points)
track_velocities.py --skipzero --average --minpoints 10 flowstream_tracks.xml
  flowstream_tracks_processed.csv

# Filter velocity vectors by position (center of chip is at 810 1024 pixels, center area
  is 40 by 40 mm2
# 940 x 940 px2, at 0.0426 mm/px => rectangle from 340, 554 to 1280, 1494)
filter_velocities.py --skip 1 flowstream_tracks_processed.csv
  flowstream_tracks_processed_and_filtered.csv 344 554 940 940

```

The resulting file **flowstream\_tracks\_processed\_and\_filtered.csv** was further processed in Excel to calculate  $\Gamma$  (see **trackmate flow field  $\Gamma$  calculations.xlsx**). Note, that on the image, the  $y$ -axis is the hydrodynamic flow axis; to keep consistency with our calculations (in which  $x$ -axis is the hydrodynamic flow axis) we swapped  $x$  and  $y$  labels in the Excel file.

**Note S7. Fabrication timeline for rectangular and circular devices**

<b>Rectangular device</b> <b>Engineering material/steps</b>	<b>Time/ Material</b>	<b>Non-orthogonal device</b> <b>Engineering material/steps</b>	<b>Time/ Material</b>
			
<b>Milling chip parts</b>			
1 × plate of PEI 1 × plate of PVC	2 × 110 cm <sup>3</sup>	1 × plate of PEI 1 × plate of PVC	2 × 110 cm <sup>3</sup>
1. Roughing bottom piece	2.5 h	1. Roughing bottom piece	2.5 h
2. Flatlanding bottom piece	1.0 h	2. Flatlanding bottom piece	1.0 h
3. Roughing top piece	1.0 h	3. Roughing top piece	1.0 h
4. Flatlanding top piece	2.0 h	4. Flatlanding top piece	2.0 h
<b>Adding fluid ports</b>			
2 × gauge 22 inlet (metal) 1 × gauge 16 inlet (metal)	2 × 10 mm 1 × 10 mm	2 × gauge 22 inlet (metal) 1 × gauge 16 inlet (metal)	2 × 10 mm 1 × 10 mm
5. Installing 2 buffer inlets	0.1 h	5. Installing 2 buffer inlets	0.1 h
6. Installing 1 sample inlet	0.1 h	6. Installing 1 sample inlet	0.1 h
<b>Adding electrical connections</b>			
platinum wire	2 × 7 cm	platinum wire	16 × 2 cm
7. Drilling 4 electrode holes	0.1 h	<b>Gold-plated nickel crimps</b> 16	
8. Preparing 2 electrodes	0.1 h	7. Drilling 32 electrode holes	1.0 h
9. Installing 2 electrodes	0.1 h	8. Preparing 16 electrodes	0.5 h
10. Gluing 2 electrodes	0.1 h	9. Installing 16 electrodes	0.5 h
11. Waiting for glue to set	2.0 h	10. Gluing 16 electrodes	0.5 h
		11. Waiting for glue to set	2.0 h
		12. Attaching crimps	1.0 h
<b>Assembling chip parts</b>			
12. Gluing pieces together	0.5 h	13. Gluing plates together	0.5 h
13. Waiting for glue to set	2.0 h	14. Waiting for glue to set	2.0 h
<b>Total time</b>	<b>11.6 h</b>	<b>Total time</b>	<b>14.7 h</b>

## Supporting References

- (1) Kochmann, S.; Ivanov, N. A.; Lucas, K. S.; Krylov, S. N. Topino: A Graphical Tool for Quantitative Assessment of Molecular Stream Separations. *Analytical Chemistry* **2021**, *93* (29), 9980–9985. <https://doi.org/10.1021/acs.analchem.1c01229>.
- (2) Schindelin, J.; Arganda-Carreras, I.; Frise, E.; Kaynig, V.; Longair, M.; Pietzsch, T.; Preibisch, S.; Rueden, C.; Saalfeld, S.; Schmid, B.; Tinevez, J.-Y.; White, D. J.; Hartenstein, V.; Eliceiri, K.; Tomancak, P.; Cardona, A. Fiji: An Open-Source Platform for Biological-Image Analysis. *Nature methods* **2012**, *9* (7), 676–682. <https://doi.org/10.1038/nmeth.2019>
- (3) Tinevez, J.-Y.; Perry, N.; Schindelin, J.; Hoopes, G. M.; Reynolds, G. D.; Laplantine, E.; Bednarek, S. Y.; Shorte, S. L.; Eliceiri, K. W. TrackMate: An Open and Extensible Platform for Single-Particle Tracking. *Methods* **2017**, *115*, 80–90. <https://doi.org/10.1016/j.ymeth.2016.09.016>.
- (4) Ershov, D.; Phan, M.-S.; Pylvänäinen, J. W.; Rigaud, S. U.; Le Blanc, L.; Charles-Orszag, A.; Conway, J. R. W.; Laine, R. F.; Roy, N. H.; Bonazzi, D.; Duménil, G.; Jacquemet, G.; Tinevez, J.-Y. Bringing TrackMate into the Era of Machine-Learning and Deep-Learning. *BioRxiv*, **2021**. <https://doi.org/10.1101/2021.09.03.458852>

## Author Contributions

S.K. suggested the design of the circular device, contributed to experimental design, performed mathematical formulation, analyzed the data, developed software, and contributed to manuscript writing. N.A.I. implemented and refined the circular device, performed experiments, analyzed data, and contributed to manuscript writing. J.C.Y.L.B. and B.I.G. helped with project conceptualization and experimental design. S.N.K. conceptualized, conceived, and guided the study, and wrote the manuscript. All authors reviewed and approved the manuscript.